1. Degree to Which Phase I Demonstrated Technical Feasibility

The Phase I program was fully successful, and all of the design goals were achieved. The accomplishments include:

- An electron gun design that provides the required beam characteristics for injection into the RF circuit.
- A design for a PPM focusing structure that demonstrates good transmission of the beam through the RF circuit and into the spent beam collector.
- Modification and detailed analysis of an RF circuit, including
  - Development of a formalism for determining the stability of overmoded klystron cavities and utilization of that formalism to determine that the cavity is stable against monotron oscillations.
  - Optimization of the cavity structure for operation at a lower voltage.
  - Realization of a RF circuit design with appropriate gain and bandwidth.
  - Performance of 3D simulations to verify that the performance is similar to conventional klystrons.
- Preliminary design of the input and output couplers and the collector, and the determination that an output window, previously developed by CCR on a DOE-funded SBIR program, will be suitable for the SBK.

Detailed results of the Phase I program are presented below.

2. Phase I Program

The primary goal of the Phase I program was to demonstrate feasibility of a sheet beam klystron capable of driving the next generation of high power accelerators and colliders.

The specific goals of the Phase I program were:

- Design an electron gun and beam focusing system capable of generating the required electron beam and transporting it through the RF circuit.
- Design an RF circuit capable of efficiently converting electron beam energy to RF energy without parasitic oscillations.
- Generate a mechanical design that is thermally and structurally robust and can be constructed at reasonable cost.

To achieve the goals given above, the Phase I Work Plan included the following tasks:

1. Determine the basic device specifications, including voltage and current limitations, duty cycle, pulse length, peak output power, and bandwidth.
2. Design the gridded electron gun.
3. Design the PPM focusing and beam transport system.
4. Design the RF circuit.
5. Design the RF windows, input and output coupling and spent beam collector.

6. Generate a preliminary, 3D solid model of the sheet beam klystron, including all major components.

These tasks were all completed successfully. In addition, issues regarding cold testing were investigated, and a method for measurement of the frequency and Q of the operating mode was developed. Detailed results for these tasks are presented in the sections that follow.

2.1. Determination of the basic device characteristics

The goal of this task was to determine the klystron's characteristics. The performance goals were

- 75-120 MW of peak RF-power
- Operation at 11.424 GHz
- Pulse length of 600 nsec - 3.2 microseconds
- Repetition Rate of 120 pulses per second

The primary independent variables are the gun impedance (or perveance), beam cross section and geometry, and number and arrangement of the cavities. The beam cross section must be compatible with the cavity. Beam focusing could be solenoid or PPM.

It was indicated in the Phase I proposal that, given the peak power requirement, a single beam device could not achieve the required specifications. Stanford Linear Accelerator Center (SLAC) proposed a dual sheet beam device consisting of two single beam devices fabricated into the same vacuum envelope. A conceptual design was shown in the Phase I proposal. This design could potentially achieve the required output power in a single device at the expense of cost and mechanical complexity. The approach in the Phase I program was to maximize the capability of the single beam device. It is anticipated that successful development of a single beam device could provide the information for a practical dual beam device.

It is clear that a study that included consideration of all cavity geometries was beyond the resources of Phase I. Furthermore, Researchers at SLAC demonstrated a computational circuit design that achieved 40% efficiency and 40 dB of gain for a sheet beam klystron operating at 490 kV. The Phase I program used this circuit design as a starting point to investigate issues related to mode conversion and low power testing of the overmoded structure. The gridded sheet beam gun currently under development served as the starting point for the proposed klystron.

The variables that remain are the beam voltage and current. A task of the program was to determine how low an impedance could be used in an SBK. This study is divided into three parts: beam generation, beam focusing (propagation) and RF circuit design.

Beam generation

Given the complexity of a full 3D gun design, beam generation is most efficiently and accurately addressed by scaling from the existing design at 415 kV. The ultimate limits in gun design are the cathode loading and the magnitude of the electric fields on the electrodes. Because a constant, DC voltage is applied to the gridded gun, it is appropriate to require an electric field of 90 kV/cm or

less at 80 kV and scale the field downward with voltage consistent with Staprans' data [1,2]. Keeping the cathode area fixed and assuming space charge limited current, we find

$$P \propto I \cdot V \propto \frac{V^{\frac{5}{2}}}{d^2} = \frac{V^2}{d^2} \cdot V^{0.5} = E \cdot V^{0.5} \qquad \text{(EQ 1)}$$

$$where E = 90 \frac{kV}{cm} \cdot \left(\frac{V}{80 kV} \right)^{-0.2}$$

To the extent that the beam compression can be increased, the current will scale with the cathode area. A plot of Eq (1) for the power scaled from the 415 kV gun is given in Figure 1. Curves are given for both the 100 cm^2 cathode area of the 415 kV gun design, and 130 cm^2. As can be seen, the power falls off slowly with decreasing voltage. For 200 kV, the 100 MW beam power of the 415 kV design can be achieved with a 20% increase in cathode area. The cathode loading as a function of voltage is shown in Figure 2. The cathode current density, even for V = 200 kV, is only 4.3 A/cm^2. A rough, 2D design of a 200 kV, 500 A gun is shown in Figure 3. 2D designs (where the beam is infinite in the direction normal to the compression plane) have been shown to be good starting points for the 3D designs.

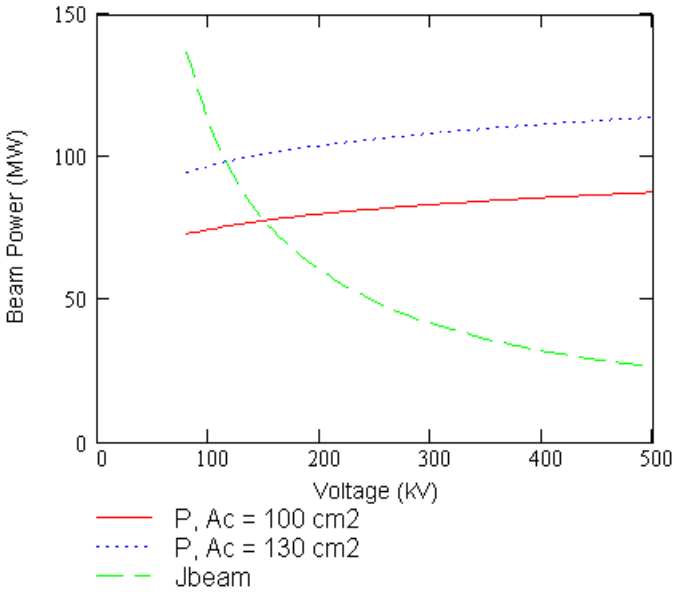

Figure 1. Dependence of beam power (left) and cathode loading (right) on beam voltage and cathode area.

Using these basic scalings, it appears that a 200 kV, 500 A gun is feasible. Some caution must be exercised, however, since these calculations do not take into account edge effects, which were a complication in the 415 kV design. Thus, a definitive statement regarding feasibility will require a complete 3D design.

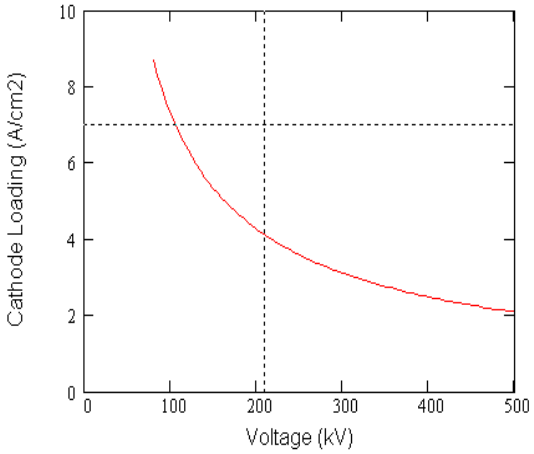

Figure 2. Cathode loading as a function of beam voltage, scaled from the 415 kV, 250 A design.

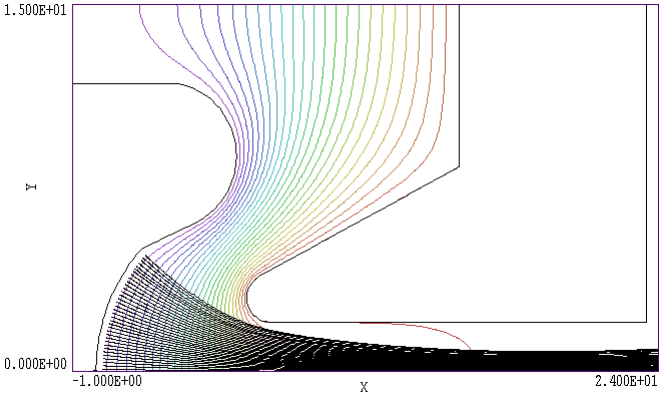

Figure 3. 2D simulation of a 200 kV, 500 A gun for a SBK.

Beam focusing

The basic requirements for PPM focusing are:

- The root mean square (RMS) value of field at the entrance to the focusing structure should be equal to the Brillouin field, increasing to about 1.5 times Brillouin in the stack.
- The field must be less than that of the "stop band" for stability. This is usually several times the Brillouin field and is not an issue here.
- The period must be less than about 0.3 times the plasma wavelength.

For a sheet beam, there is the added complication of confining the beam in two dimensions in the presence of edge fields. This is addressed in detail below. Using the same scaling as discussed above, the Brillouin field can be shown to be

$$B_B = \sqrt{\frac{\frac{P}{W \cdot \delta r}}{0.924 \cdot 10^6 \cdot V^{1.5}}} \qquad \text{(EQ 2)}$$

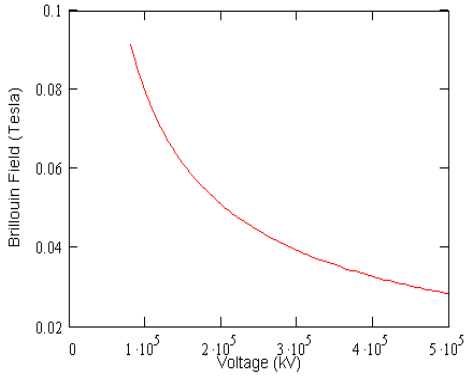

Figure 4. Brillouin field as a function of voltage, for the scaling of equation 2

where W and δr are the width and half-thickness of the beam, respectively. This is plotted in Figure 4. It can be seen that 1.5 times the Brillouin field is easily achievable with inexpensive ceramic magnets. Again, however, edge effects will be of increasing importance with higher current density.

RF structure

For high power klystrons, increasing the perveance will typically result in a reduction of the efficiency due to space charge debunching. The SBK is, of course, not immune to this phenomenon. However, as shown in Figure 2, the current and space charge density in the SBK is roughly 1/30 of that of a conventional klystron. Figure 9 demonstrates the impact of perveance, and hence space charge density, on efficiency in high power klystrons.

The perveance for the klystron considered in Figure 2 is 0.75 μPervs. From Figure 5, it is clear that reducing the perveance by a factor of even 2 would produce a dramatic increase in efficiency. Note that the usual definition of perveance cannot be applied meaningfully to a sheet beam, since the width and thickness are independent. But, for fixed voltage, it would be expected that the change in efficiency as a function of current (and space charge) density should be about the same as shown in Figure 5.

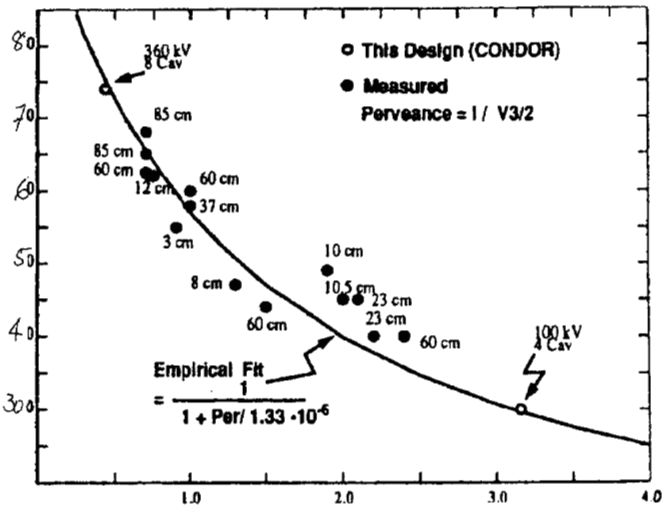

Figure 5. Efficiency (%) versus perveance (micropervs) for a range of klystrons. From G. Caryotakis, unpublished class notes.

This ignores other differences in the SBK compared to conventional klystrons. For current designs, the gain per unit length appears lower and the effect of space charge appears higher. For a given gain, the length of the SBK RF structure is roughly 2-3 times longer than for an equivalent conventional klystron. It will be necessary to decrease the charge density by 4-9 times to keep the ratio of plasma wavelength to RF structure length constant. Thus, the SBK's effective reduction in current density (and perveance) is more like 1/3 - 1/7.

Nevertheless, Figure 5 implies the 415 kV and 250 A SBK design is well within the range where space charge effects are small. Conversely, the argument is made that the perveance per unit area, commonly referred to as perveance per square, can be increased by a factor of 3 - 7 before there is a significant decrease in efficiency. At 200 kV and 500 A, the perveance per square is 6 times that for operation at 415 kV, 250 A. Given that the RF structure will be shorter and the effect of

plasma density somewhat reduced, the efficiency is expected to be adequate. Of course, a detailed design and simulation is required before a definitive statement can be made.

Conclusion

Based on straightforward scalings, a 50 MW, X-Band, sheet beam klystron is feasible with a beam voltage of 200 kV. It is CCR's experience, however, that edge effects, both in the beam and the PPM structure, must be carefully considered. A definitive statement on lower voltage operation will require a careful 3D analysis.

2.2. Electron Gun

The electron gun development utilizes the design currently being constructed with existing DOE funding. The design was refined to improve beam quality to ensure compatibility with good transmission using PPM focusing.

Extensive simulations were performed using the 3D trajectory code OmniTrak. OmniTrak is a commercial code from Field Precision and incorporates the physics required for this simulation, including the full 3D calculation of the self magnetic field.

Two important changes were made. The first was to change the electric field stress distribution so that the intermediate electrode, or modulating anode, shields the cathode against breakdown. This was achieved by moving and reshaping the intermediate electrode so that it played a significant role in the formation of the beam, rather than just following equipotentials defined by the simple diode. This allowed an increase in the cathode to anode distance to reduce the field stresses on the anode and downstream side of the intermediate electrode. Consequently, if breakdown occurs, it will be between the cathode and the intermediate electrode. Since the intermediate electrode does not normally carry current, it has a high impedance connection to the power supply. Thus, little energy can be delivered to an arc. During breakdown the intermediate electrode will collapse to the cathode potential, increasing electric fields between the anode and intermediate electrode. In the new design, the distance between these electrodes is sufficient to avoid breakdown. Figures 6

and 7 show 2D simulations of the old and new designs. A 3D drawing of the new design is shown in Figure 8.

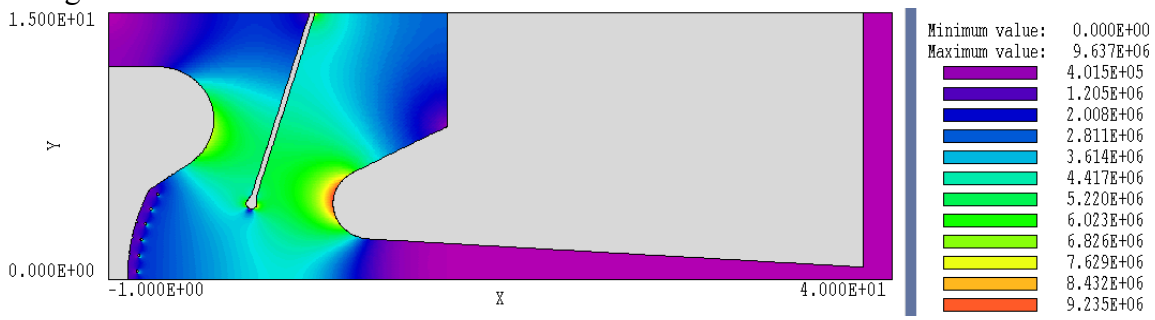

Figure 6. Previous design, with the "neutral" intermediate electrode position.

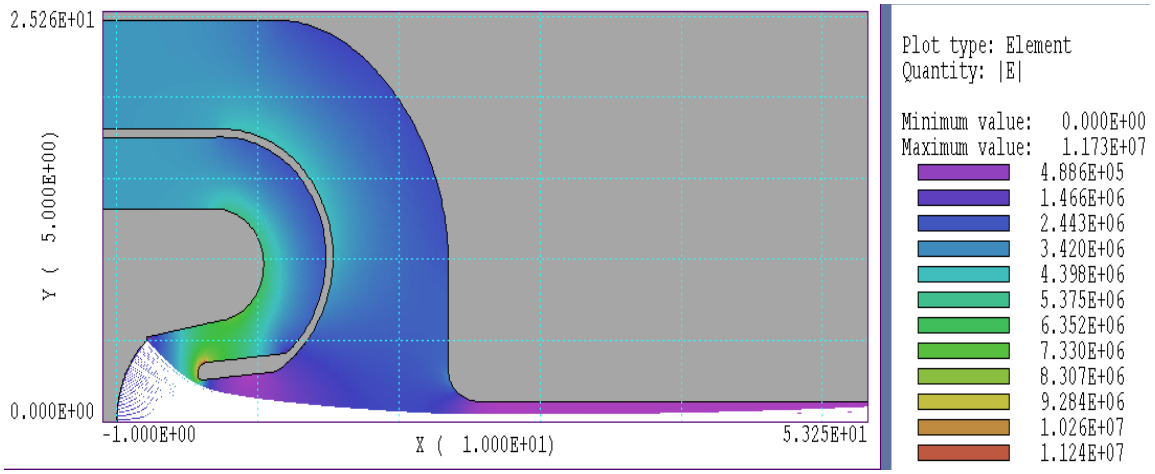

Figure 7. New design, with the more aggressive intermediate electrode and greatly reduced field stresses between the intermediate electrode and anode.

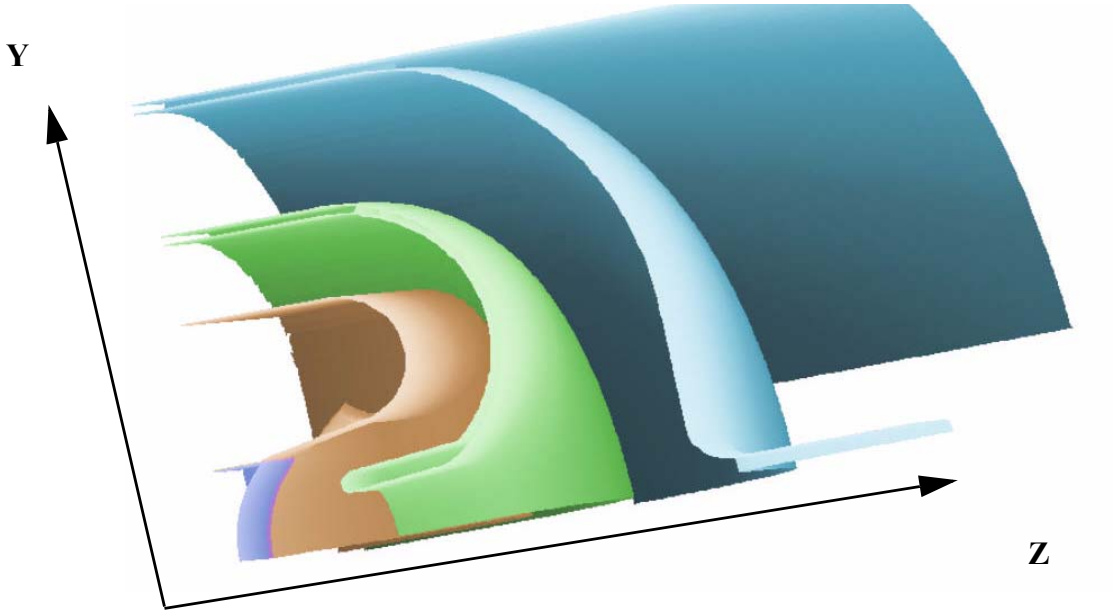

Figure 8. New design for the electron gun. One fourth of the gun is shown.

The second improvement was to change the contour of the cathode focus electrode to improve the beam quality. This was particularly important for trajectories starting near the outer corners of the emission surface where edge effects are strongest. The new focus electrode is shown in Figure 9.

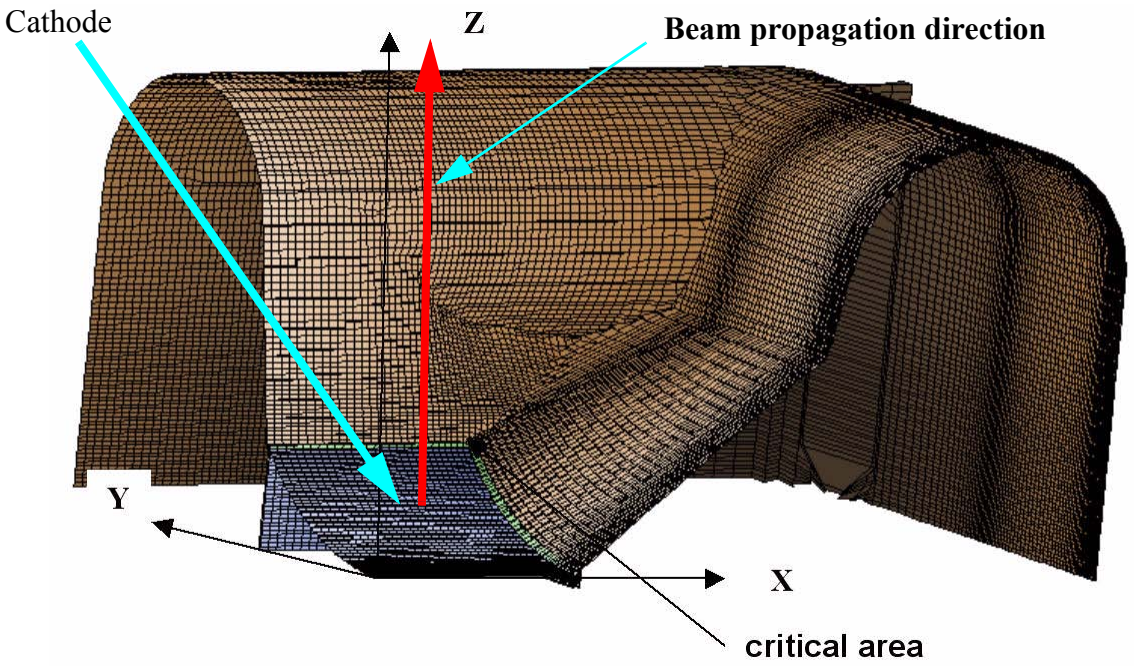

Figure 9. Detail of the cathode focus electrode. The electrode has complex contouring in the corner to correct for edge effects. Beam propagation is in the Z-direction.

Results of the simulations of the gun are shown in Figures 10, 11 and 12.

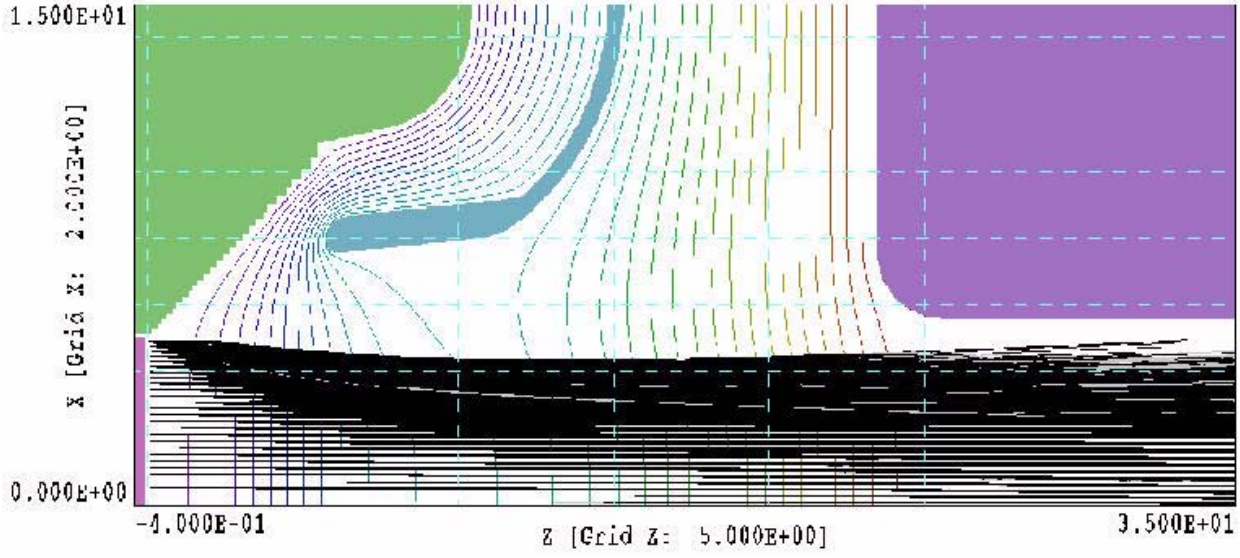

Figure 10. Beam in the XZ (non-compression plane). Dimensions in cm.

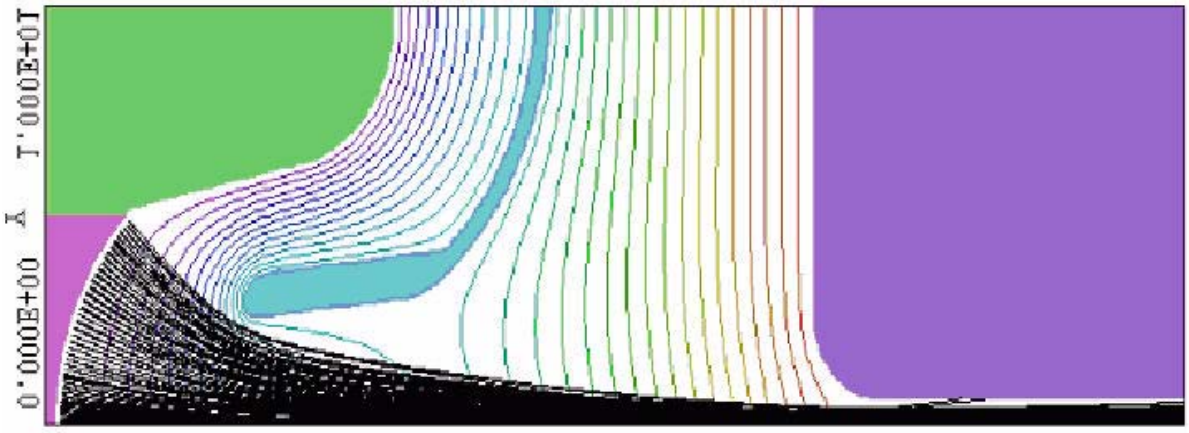

Figure 11. Beam in the YZ (compression plane).

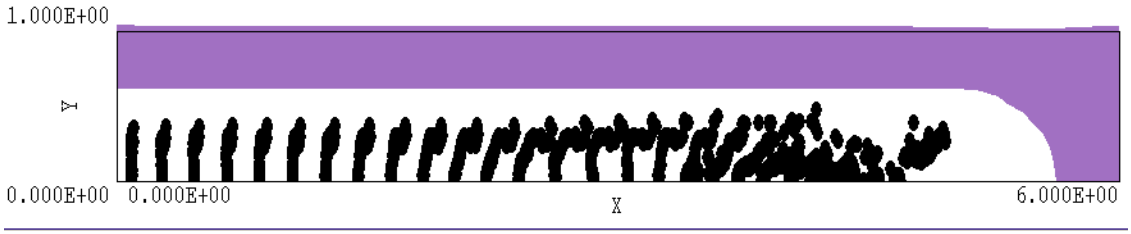

Figure 12. Distribution of the beam trajectories at the XY plane at the waist, 25 cm from the cathode. (Quarter problem shown, as modeled.)

The beam appears well formed except for the very corner. Approximately 10 A strike the anode. This level of current can be handled with proper cooling. However, as discussed below, there are difficulties in propagating the beam associated with a spread in the Y momenta. A P_y versus Y phase space plot is shown in Figure 13. The bulk of the trajectories fall within a distribution of +/- 30 mrad which, as discussed below, propagate through the PPM stack. There are a significant

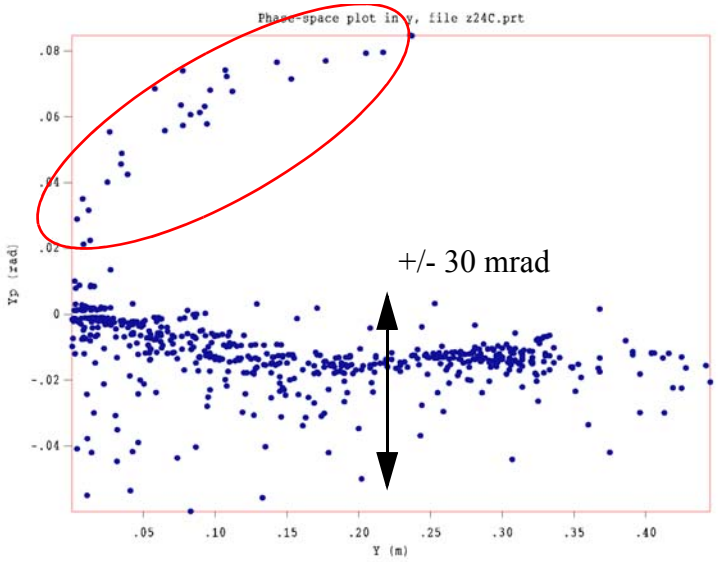

Figure 13. Y Phase space distribution of the beam from the electron gun (without magnetic field). The distribution is taken just upstream of the waist. The problematic rays are circled.

number of rays, however, that fall far outside of this range. This problem was noticed only after studying the propagation in the PPM stack. Further design refinements should reduce the number of rays with high Y momenta to an acceptable level. This will be performed in the existing electron gun development program.

These simulations do not include the control grid; however, the grid is intended to be non-perturbing when the beam is extracted. The grid can be accurately simulated in 2D, because it is close to the cathode and high resolution mesh sizes can resolve the grid wires with reasonable simulation times. The electron gun development program achieved a cathode-grid design demonstrating excellent beam quality. Once the gun design is finalized, the grid will be included in the 3D simulations to verify proper operation. Figure 14 shows a 2D simulation of the electron gun with the control grid.

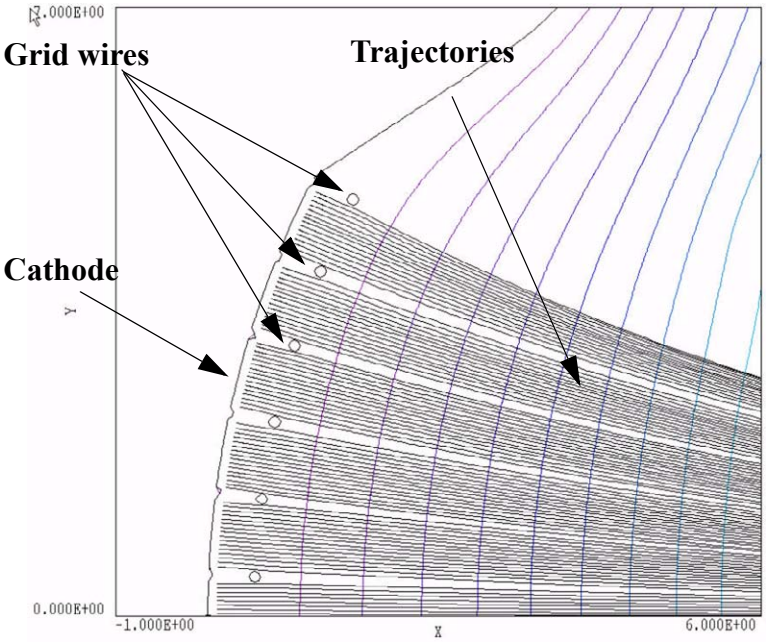

Figure 14. 2D simulation of the sheet beam gun with control grids

2.3. Design of PPM Focusing Structure

The sheet beam klystron incorporates a PPM focusing structure. Studies by Booske *et al*.[3] indicate that either PPM or wiggler focusing is feasible for the SBK. PPM was chosen because of the existence of calculations by Booske *et al.*[4] and Basten *et al.*[5] on configurations specifically for sheet beams. Those configurations include those shown in Figure 15.

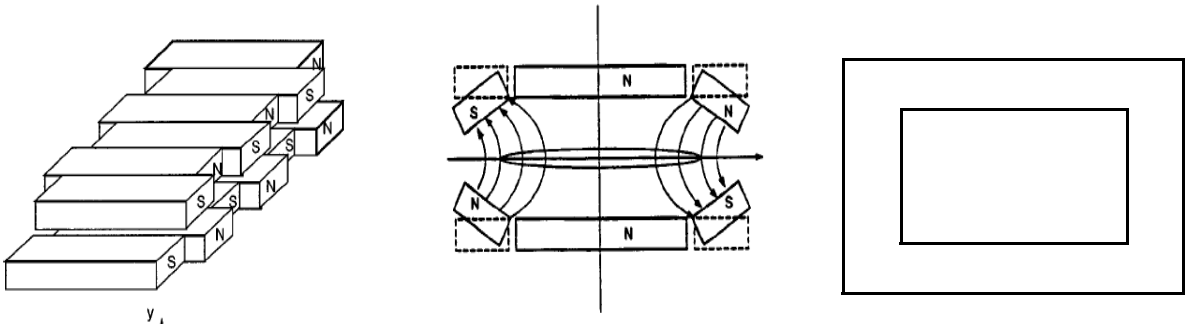

Figure 15. Three configurations for PPM focusing structures for sheet beams. From Refs. [4] and [5].

The fundamental aspects of the PPM structure, specifically the field and period, can be determined using methods developed for round beams [6]. These methods are generally not relativistic, and specifically do not include the effects of self magnetic fields. Accordingly, a formalism was developed and numerical calculations performed to obtain the required field and period for focusing in the direction normal to the wide plane of the beam (*i.e.*, the plane comparable to the r-z plane in a cylindrical device). The results are shown in Figure 16.

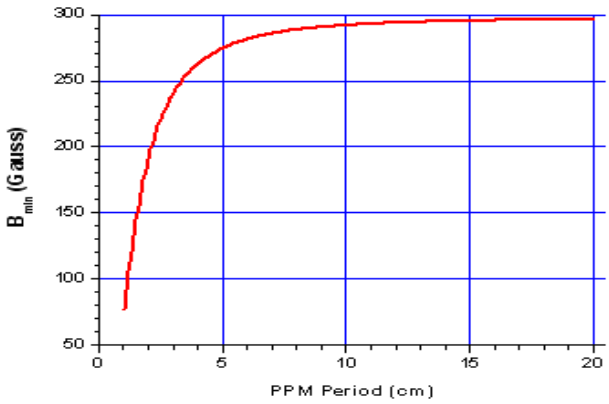

Figure 16. Minimum field for confinement, and field for injection for the 415 kV beam of the SBK as a function of the magnet period for a non-immersed cathode. The red curve is applicable to the SBK.

For a 10 cm period, the peak field is 280 G, or an RMS value of 198 G. The non-relativistic Brillouin field for a sheet beam is given by [7]

$$B_B := \sqrt{\frac{\frac{I}{W \cdot \delta r}}{0.924 \cdot 10^6 \cdot V^{0.5}}} \qquad \text{(EQ 3)}$$

where now B_B is the RMS value. W and δr are the beam width and 1/2 thickness, respectively, and V and I are the beam voltage and current. For the SBK, B_B = 320 G. The relativistically correct value is significantly lower than that given by Equation (3).

From Ref. [6], the period should be no more than about 0.31 times the plasma wavelength, which is 30 cm. Since it will be necessary to fit cavities into the PPM stack, we have chosen the longest period: 10 cm.

All of the configurations shown in Figure 15 will provide focusing in the Y plane. Figure 15a provides no focusing in the X plane; however, this is achieved with the configurations shown in Figures 15b and 15c. Basten found good propagation with c with very thin, elliptically shaped beams[5]. Unfortunately, as pointed out in Ref. [4], beams of appreciable thickness will be distorted near the edges with X plane focusing producing curling of the edges in the Y plane.

The other issue is matching of the beam into the focusing field. Since the effective plasma frequency near the edges is a function of the distance from the edge, achieving a match requires a gradient in the magnetic field in the X direction. This tends to induce distortion. Fortunately, the beam for the SBK has a relatively low current density, and these space charge induced effects can be balanced.

The best result is achieved with a combination of configurations of Figures 15 b and c. The configuration shown in Figure 17 utilizes bar magnets that are continuous in the Z direction (direction of beam propagation) to provide a field in the Y (vertical) direction. This provides a cycloidal

motion in the XZ plane that, for weak fields, results in a shallow arc. With the proper polarity, the arc opposes the outward drift in the X direction.

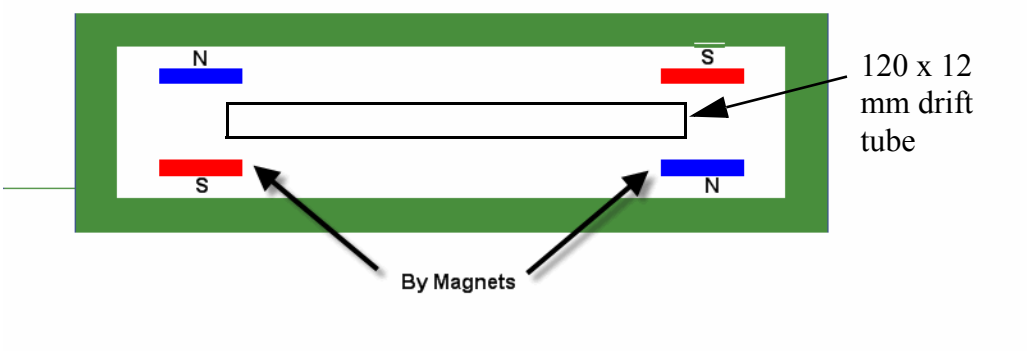

Figure 17. Cross section used for the magnet.

The PPM structure used in the SBK is shown in Figure 18.

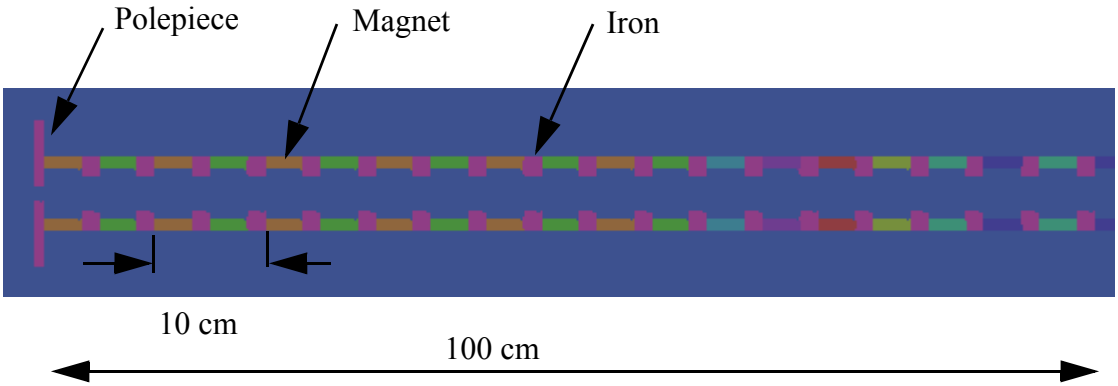

Figure 18. PPM structure (YZ plane).

The magnetic field is given in Figure 19. The RMS field at the entrance is approximately the (relativistically corrected) Brillouin field, rising quickly to about 1.5 times that value. The field is then tapered upward along the axis so that it is highest at the output cavity to handle defocusing due to RF-induced space charge fields.

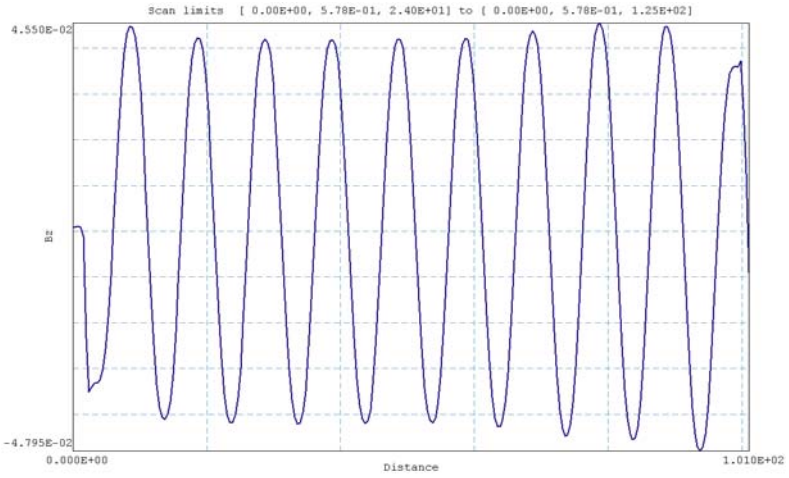

Figure 19. Magnetic field, Bz, along the center of the PPM structure, as a function of Z. Distance is in cm. Field is in Tesla.

Omnitrak simulations of a simulated beam with no velocity spread demonstrated 100% transmission through the PPM structure. The beam was minimally distorted and well focused in both planes, as shown in Figure 20.

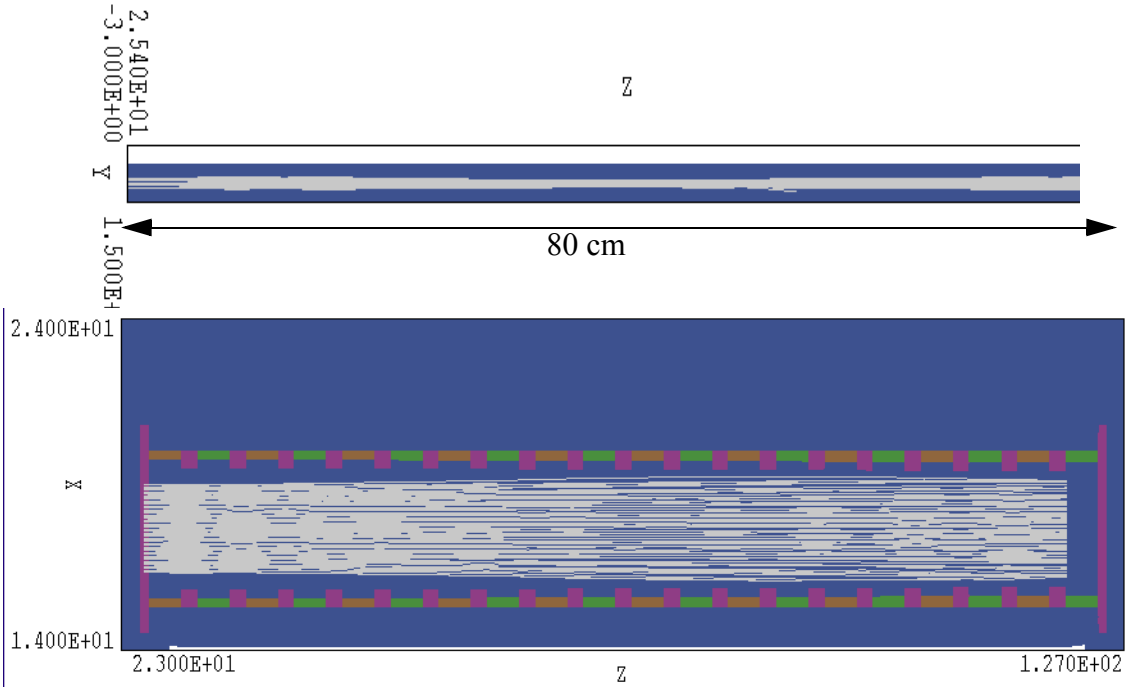

Figure 20. Omnitrak simulation of an ideal beam through the PPM structure. Top, middle, bottom: YZ, XZ and XY planes. Good focusing was achieved in both planes, and the transmission was 100%.

To verify proper operation with the existing gridded electron gun design, the simulated beam from the gun was injected into the PPM focused structure. These results indicated relatively poor performance, with only 94% transmission. The reason became clear upon inspection of the beam phase space. Although the beam appears reasonably laminar in real space, Figure 13 indicates there is a significant portion of the beam with high momenta in the Y plane. This was not evident prior to the “test” with the PPM stack. Fortunately, the problem appears correctable by reshaping of the focus electrodes, and this will be performed in the existing gun development program.

To give assurance that the corrected beam will indeed propagate with minimal interception, a beam with the expected spread of +/- 30 milliradians was injected into the PPM structure. The resulting trajectories and final distribution are shown in Figures 21 and 22, respectively. Please note the comments in the figure caption regarding the visual display. The predicted transmission is 99.6%.

In summary, the analytical calculations and 3D simulations indicate that, if the beam has a reasonable velocity spread, good beam transmission can be achieved with PPM focusing.

.

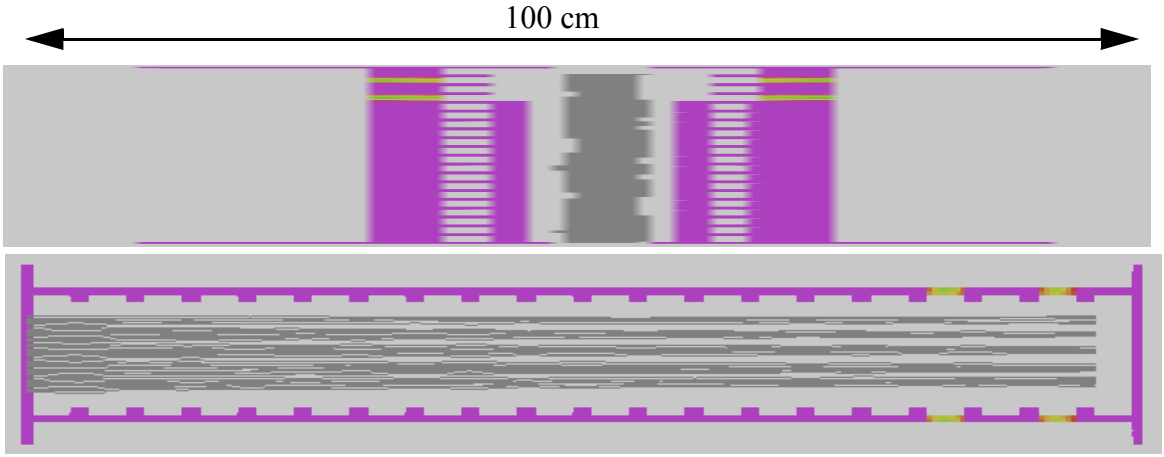

Figure 21. Trajectories of the simulated beam with a +/- 30 mrad distribution.

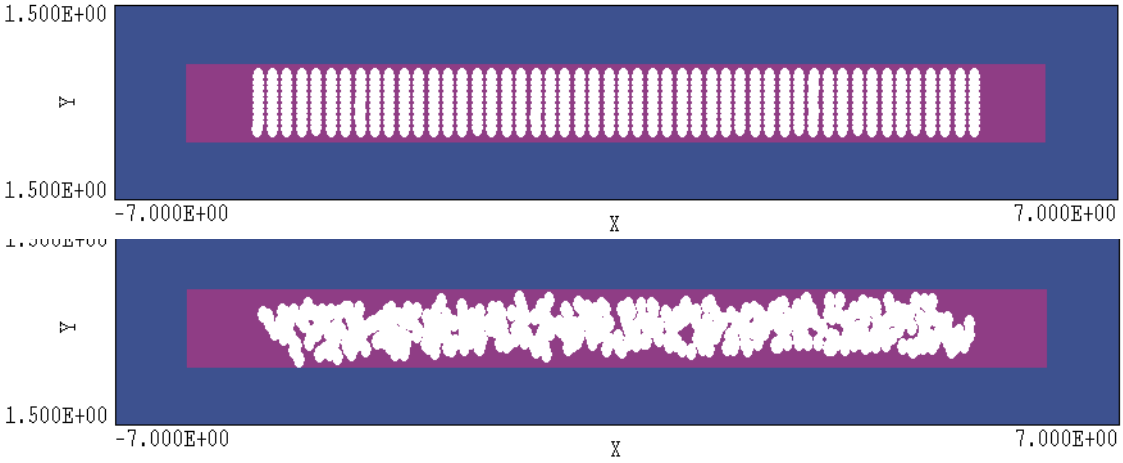

Figure 22. Initial (top) and final (bottom) beam distributions for an artificial beam with +/- 30 mrad angular spread, simulating the expected distribution of the beam from the corrected electron gun. The visual display is deceptive in that the performance is better than it appears. The large diameter of the circles representing the beam give the impression that the beam extent is greater than predicted. The actual fill factor of the initial beam, for example, is only 67%, although it appears more like 80 %. The beam transmission was 99.6% after 80 cm.

2.4. RF Circuit Design

Geometry and Linear Calculations

The initial RF circuit design was provided by Stanford Linear Accelerator Center[8]. The design includes five cavities, with all but the input being three-cell, extended interaction cavities. There were two primary tasks in the design. The first was to calculate the gain, bandwidth and efficiency assuming the cavities are operated in the fundamental mode. The second was to determine whether there would be competing, higher order RF modes that could disrupt circuit operation. The second was viewed as the highest risk issue for the program, and considerable resources were

devoted to its investigation. Fortunately, as will be shown below, mode competition does not appear to be a problem.

Previous research [9] demonstrated that one of the difficulties with cavities for a sheet beam klystron is the weak ratio of beam coupling to stored energy, or R/Q. To increase the R/Q, multi-cell, or extended interaction, cavities were used for all of the cavities except the input. The three-cell geometry is shown in Figure 23. As done by others [9,10], a re-entrant section was added at each end of the cavity to flatten the field profile along Y in the main portion of the cavity.

The parameters of this cavity were optimized for operation with the 415 kV, 250 amp operation of the CCR gridded gun. In addition, the re-entrant regions were modified to flatten the electric field profile and increase the R/Q.]]

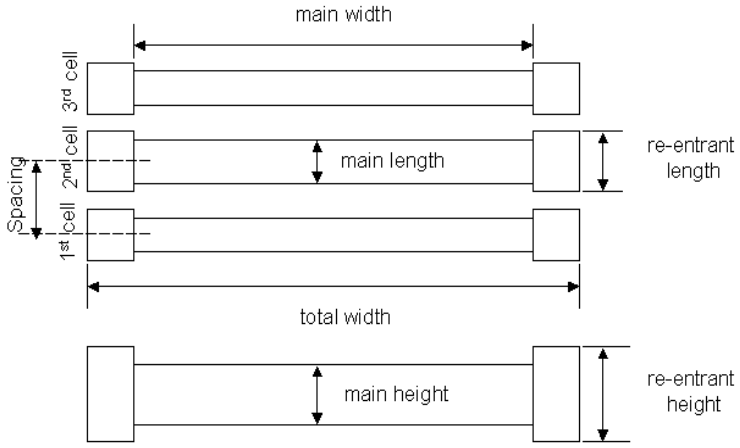

	Cell 1/3	Cell 2
Total Width	127.40	127.40
Reent Length	7.65	9.18
Reent Height	22.49	22.49
Main Width	104.50	104.50
Main Length	5.10	6.63
Main Height	18.07	18.07

Figure 23. Cavity geometry.

Mode patterns for the cavity, as calculated using 3D MAGIC, are shown in Figures 24 and 25. The distribution along Z reflects the π mode, which provides maximum coupling to the beam.

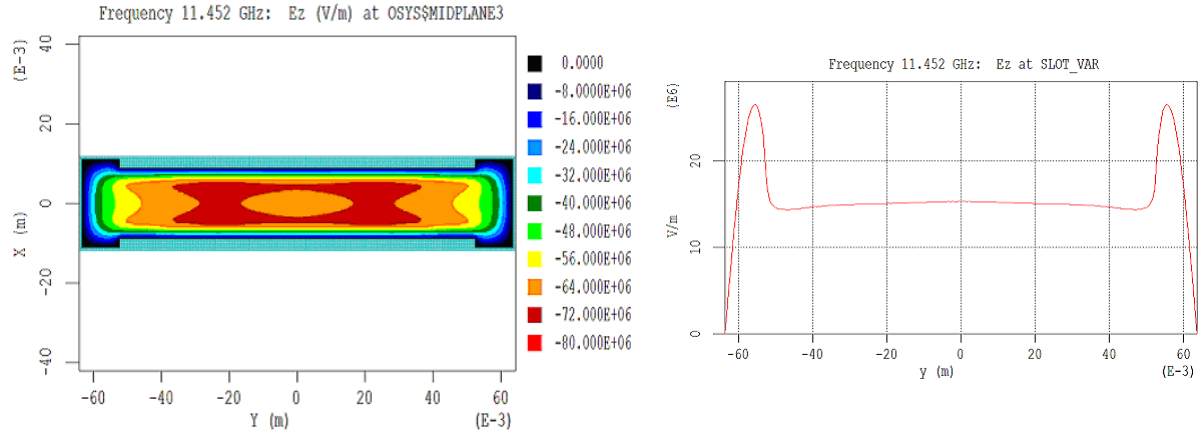

Figure 24. (Left) Ez on the XY plane at Z=0. (Right) Plot of Ez versus Y at X =0. Note that for all of the cavity plots, X and Y correspond to Y and X, respectively, in the gun and ppm structure plots.

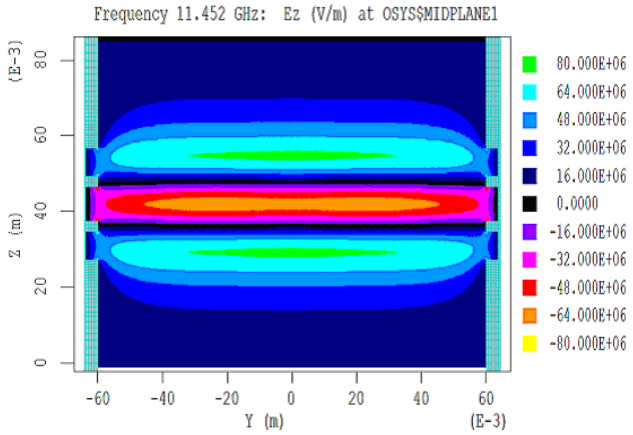

Figure 25. Ez on the YZ plane at X = 0.

The small signal gain and bandwidth were calculated using formulas commonly employed for cylindrical klystrons with modifications to the coupling factors and the reduced plasma frequency. A MathCad^{TM} program was adapted from a program used by SLAC for cylindrical klystrons. The code requires the cavity resonant frequency, Q, and R/Q. These were determined from the MAGIC simulations that produced the field patterns shown above. The cavity frequencies, axial positions and loaded Qs were varied to optimize the gain for a bandwidth of 20 MHz. This bandwidth should be adequate for gridded operation where pulse compression is not required. A plot of the gain as a function of frequency is shown in Figure 26, and the cavity parameters that were used to achieve that gain are shown in Table 1. The results are comparable to those of a conventional klystron.

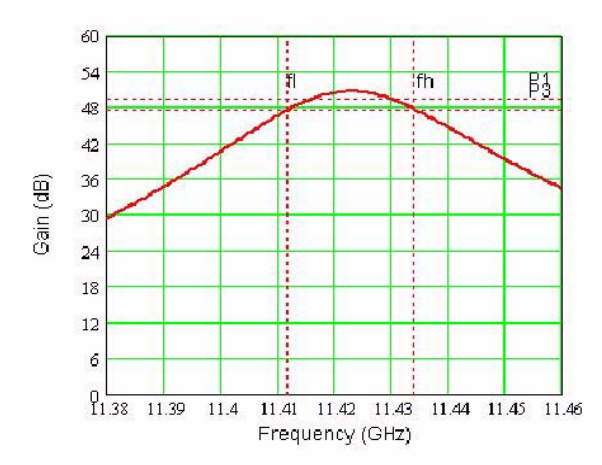

Figure 26. Gain of the klystron. The 3dB bandwidth is 0.2%.

Table 1. Cavity Parameters

Cavity	Freq. (GHz)	Q_L	Position (m)
1	11.424	500	0.0
2	11.418	500	0.22
3	11.575	500	0.50
4	11.70	500	0.64
5	11.424	250	0.78

Mode Competition

The SBK cavities are single-moded in the short dimension but can have many variations across the wide (Y) direction near 11.4 GHz. The transverse patterns for the TM_{11} and TM_{31} modes are shown in Figure 27.

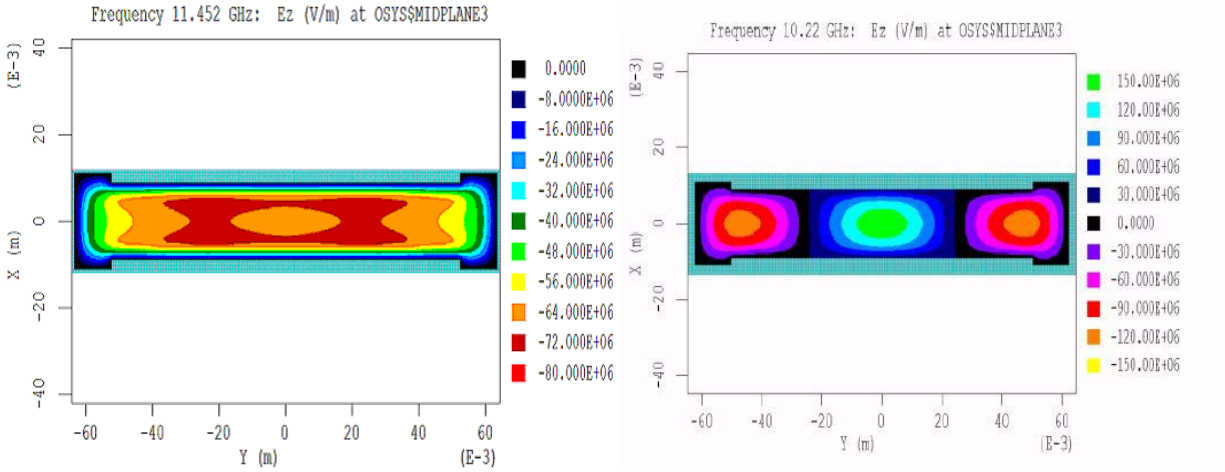

Figure 27. Transverse mode patterns for the TM_{11} (left) and TM_{31} modes (right).

Because there are three cells for each cavity, there are three field variations that can exist in the Z direction. These are shown in Figure 28. The spacing between the cells of the cavity are such that the π mode has the strongest interaction with the beam and is thus chosen for operation. mode.

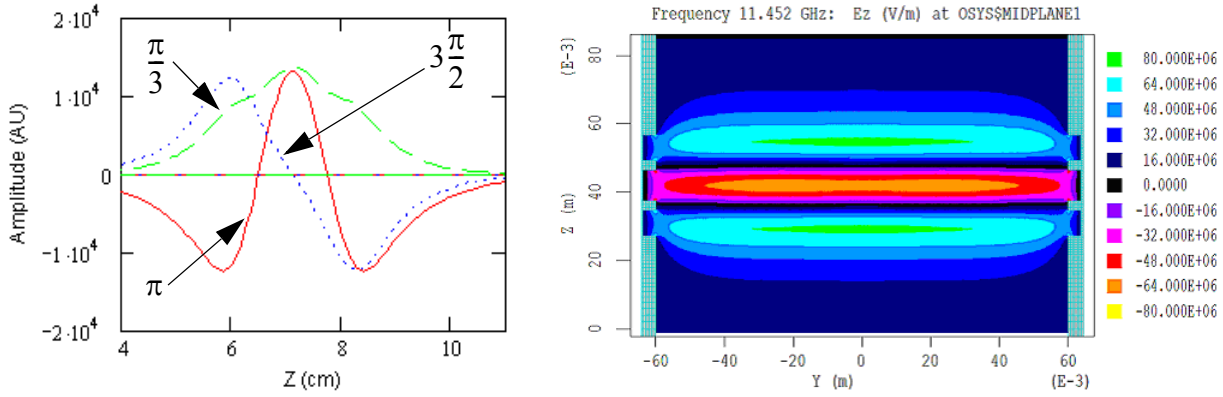

Figure 28. The left plot shows Ez as a function of z for the three "axial" modes of the penultimate cavity. The right plot shows the fields in the XZ plane for the pi mode.

Y Eigen-number	Axial Pattern	Frequency (GHz)
0	+-+	11.4255
2	+-+	11.487
3	+-+	11.662
4	+-+	12.006
5	+-+	12.433
1	+++	9.7442
2	+++	9.876
3	+++	10.142
4	+++	10.542
5	+++	11.062
1	+0-	10.7113
2	+0-	10.782
3	+0-	10.997
4	+0-	11.361
5	+0-	11.829

Figure 29. Modes of the SBK three-cell cavities.

The modes in that can exist in the penultimate cavity are given in Figure 29. The principal concern was that a parasitic, competing mode would oscillate and disrupt operation of the klystron. To address this concern, CCR developed a computer code to calculate the start currents of these competing modes.[11] This was the most critical task of the Phase I program.

Except for the mode with negligible variation across the Y direction, the coupling to the beam is essentially the same for all Y eigenvalues. This is definitely not the case for the axial mode profiles, and the calculations focused on this effect. The start current code integrates the electron energies through the fields of the cavity using conventional equations of motion. Some effort was made to find an analytic approximation using Hermite Polynomials for the variation of the fields along the axis. It was found, however, that this underestimated the tails of the field distributions and underestimated the start current. For this reason, the code uses profiles calculated by MAGIC.

Results of the calculations are shown in Figures 30 and 31. All but four of the modes exhibit negative start currents and thus are stable for all currents. With the loaded Qs given in Table 1, the lowest starting current is 400 A, or about 1.5 times the operating current. **This indicates that the klystron is stable against oscillations for all modes.**

Mode y eignennum	variation	Frequency	Start Current (A) Q=500
1	+++	9.791	-1,410
2	+++	9.935	-1,515
3	+++	10.216	-1,479
4	+++	10.643	10,320
5	+++	11.201	-1,515
6	+++	11.867	-3,765
0	+-+	10.701	-765
2	+-+	10.814	-4,140
3	+-+	11.054	-2,850
4	+-+	11.452	-4,980
5	+-+	11.97	1,935
6	+-+	12.548	5,595
1	+0-	11.421	-32
2	+0-	11.507	395
3	+0-	11.717	-72
4	+0-	12.101	975

Figure 30. Data for the calculations of start current.

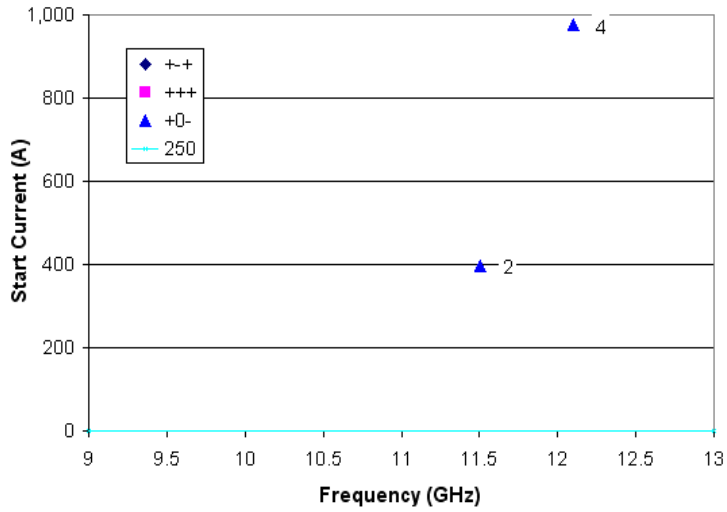

Figure 31. Start currents of competing oscillations in the penultimate SBK cavity. The labels indicate the Y eigennumber.

The other concern is whether higher order modes will be excited and amplified by non uniformities in the beam. The mode closest to the operating mode, TM_{02} +-+, oscillates 62 MHz from the operating frequency. This appears to be a large enough separation in frequency, and this is confirmed by the absence of significant distortion in mode pattern in the MAGIC simulation shown in Figure 27. (Experience with overmoded waveguides for gyrotrons has shown that the mode pattern will be very visibly distorted with the presence of even 10% of a high order mode.)

Efficiency

The efficiency was calculated using a full 3D simulation with MAGIC. The simulation used the cavity parameters given in Table 1 and a simulated beam with a uniform 0.3 Tesla magnetic field. All simulations were run to equilibrium, between 30 ns and 40 ns. The simulation was executed in two stages: the first included all but the output cavity, while the second contained just the output cavity with the beam from the first stage. This allowed optimization of the output cavity loaded Q without re-running the entire simulation. A full simulation requires approximately 48 hours on a state-of-the-art personal computer.

The geometry and beam for the first stage are shown in Figure 32. Outputs from the first part are shown in Figures 33 and 34. The surface and line integrals of the RF current and the gap field are shown in Figure 34. The mode patterns are very close to those calculated without the beam, and the mode appears to be essentially pure TM_{113}.

The peak ratio of RF to DC current is 1.4; however, the peak occurs upstream of the output cavity (the end of the first section.) This can be corrected through adjustment of the frequency offsets and spacings of the third and penultimate cavity. In addition, an RF/DC current ratio approaching 1.6 should be achievable. This optimization will be accomplished in the Phase II program.

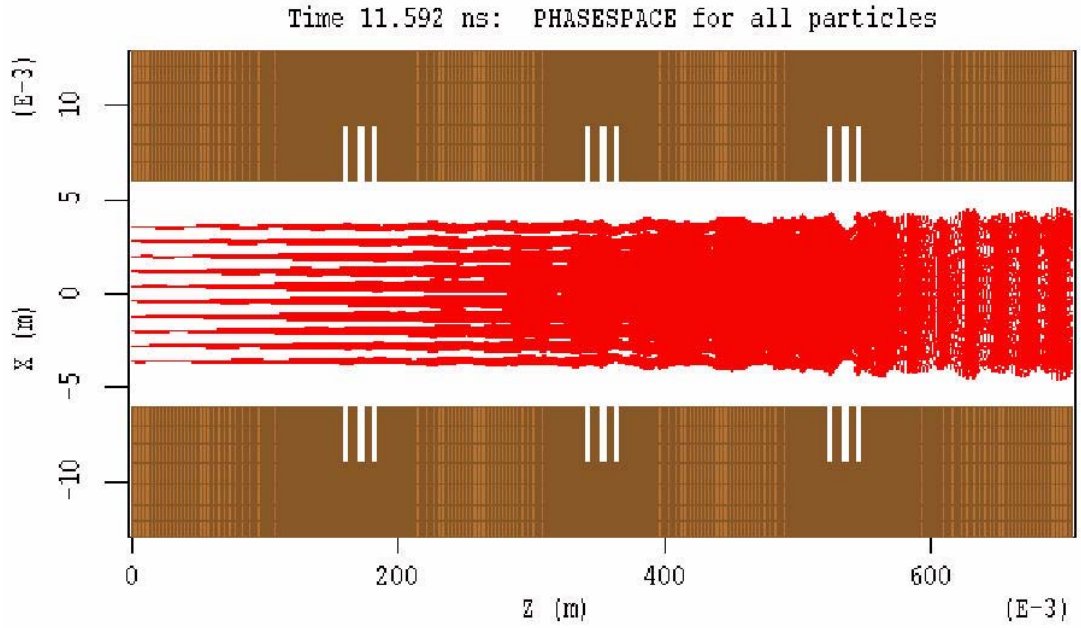

Figure 32. Output from the first stage of the MAGIC 3D simulation of the SBK. This stage contains all but the output cavity.

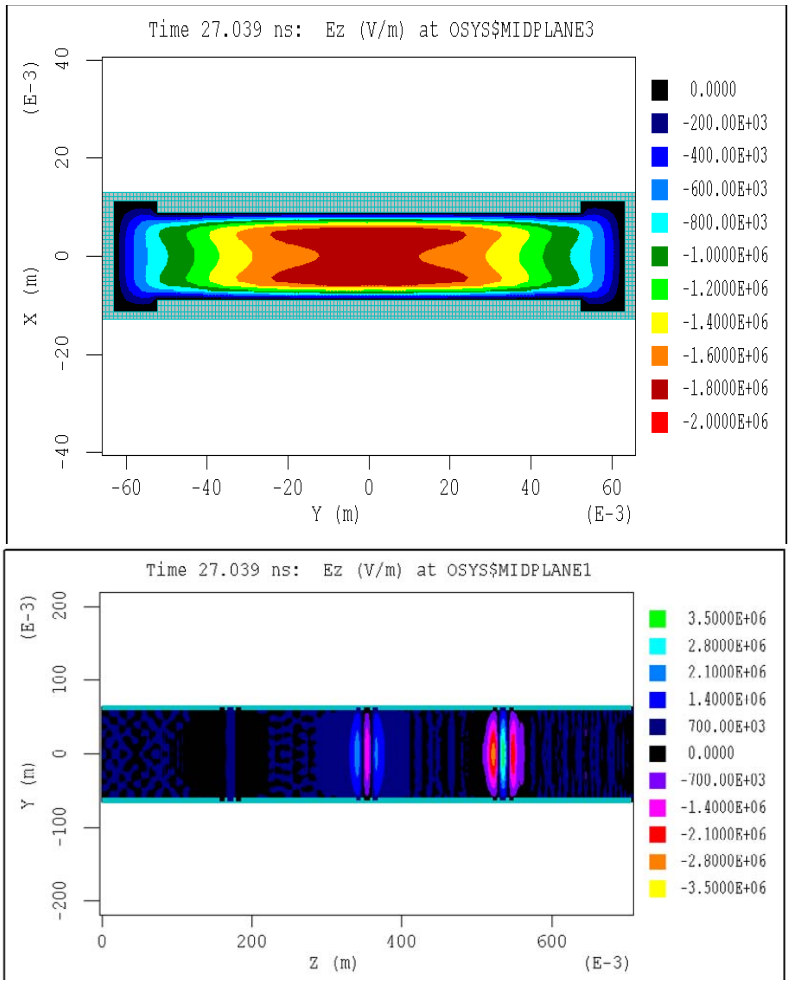

Figure 33. Top: RF Ez amplitude contour on the XY plane of the 3rd cavity. Bottom: YZ plane.

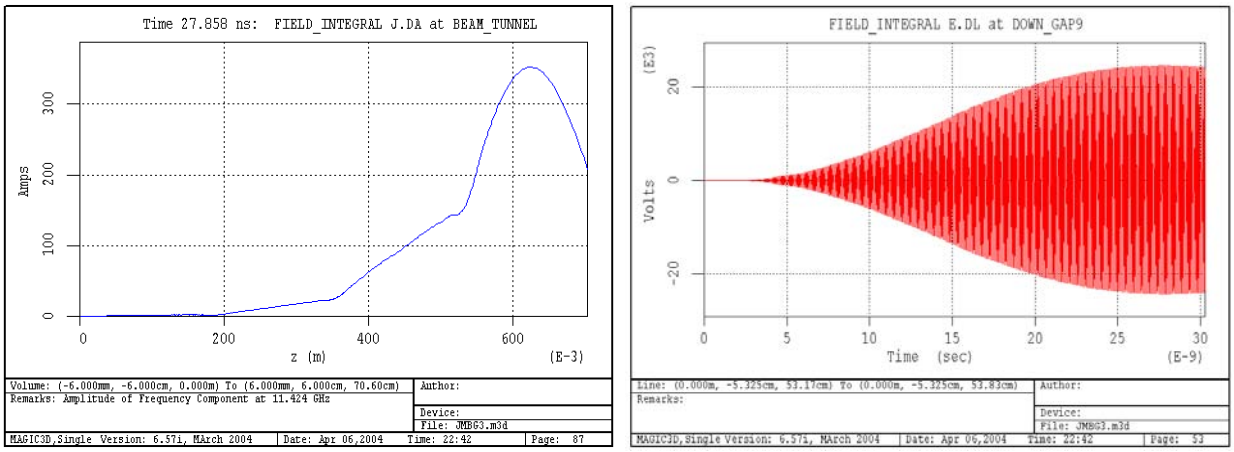

Figure 34. Outputs from a 3D simulation: (Left) The left plot shows the integral of the current density over the beam area at the penultimate cavity. The right plot shows the integral of the electric field at the last cell of the 4th cavity.

Optimization of the entire klystron structure was beyond the scope of Phase I. Instead, an artificially bunched beam was injected into the output cavity to estimate the efficiency. Without optimization of the output cavity other than selection of the loaded Q, a power of 50 MW and an efficiency of 48% were achieved. This is shown in Figure 35.

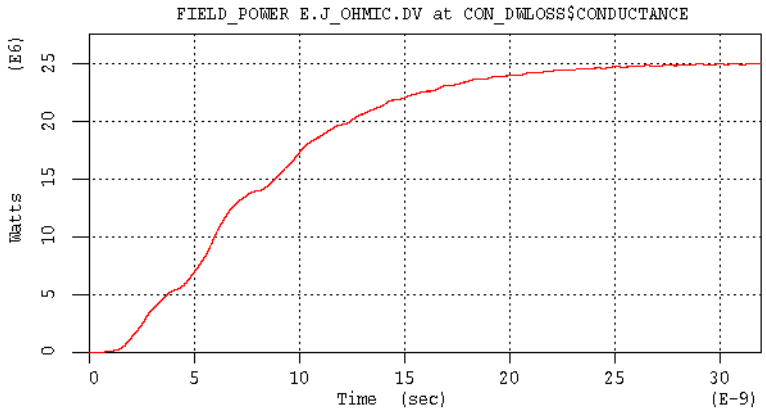

Figure 35. Power in one of the two loads in the output cavity, using a prebunched beam.

Cavity Sensitivity and Tuning

The cavity resonant frequency is sensitive to dimensional changes as shown in Table 1. The most sensitive dimension is that of the main (center) portion of the cavity. The sensitivity to height is particularly high at 0.7 MHz/micron. For a system where the Qs are approaching 700, the resonant frequencies should be accurate to significantly less than 16 MHz, which requires a tolerance of better than 22 microns, roughly 0.001 inch. While machining tolerances to about 0.0001 inch can be obtained with the shapes of interest, it becomes rather expensive. Tuning the cavity after fabrication is a better option and adds the ability to change cavity frequencies to optimize performance. It should be straightforward using a clamping arrangement to vary the height of the main portion of the cavity. It is anticipated that deformations up to a few 10s of microns can be achieved without significantly perturbing the mode pattern or exciting higher order modes. Tuning of the height will also compensate for small dimensional errors in the spacing.

Table 1. Frequency sensitivities of three-cell cavities.

Dimension	Frequency (MHz/mm)
re-entrant width	-9.70
re-entrant height	-6.245
main width	+18.00
main height	-660.0
main length (1st cell)	-156.0
main length (2nd cell)	+70.0
spacing	+223.0

2.4.1. Design of the RF windows, input and output coupling and spent beam collector

RF Windows

The RF window is based on an existing CCR design and consists of a window in circular guide coupled to WR90 rectangular waveguide by wrap-around mode converters. These elements are shown in Figure 36. The window is designed to transmit 100 MW of peak power. These windows are in operation on the X-Band magnicon at the Naval Research Laboratory. The return loss for the window/mode converter combination is shown in Figure 37. These results indicate that the return loss is less than 30 dB around the operating frequency.



Figure 36. Left: 100 MW XBand output window. Right: Wrap-around mode converter to go from the input and output of the window.

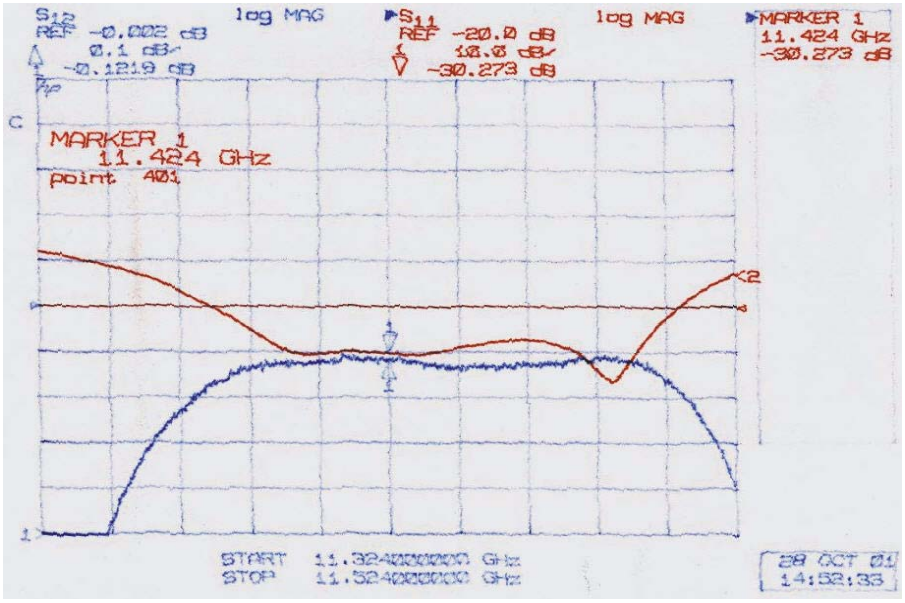

Figure 37. Network analyzer results for CCR 100 MW window at 11.424 GHz. Over a bandwidth of 100 Mhz, S11 is -30dB and S12 is -0.15 dB.

Input and Output Couplers

Coupling is possible through the top (YZ) and side (XZ) planes of the circuit. Both were investigated for input and output coupling. Top coupling provides a large area so the power density in coupling holes or slots would be modest; however, this must be balanced against mode purity. In principle, the large area facilitates matching of the phase and amplitude to a specific mode. A rectangular guide that is end-coupled into the top of the cavity is the most flexible. The fields of a TE_{10} waveguide mode have the same phase as the desired cavity mode, and an array of holes or slots with varying dimensions can be used to match the amplitude. A MAGIC simulation of a five-slot coupler is shown in Figure 38. This design had nonuniform coupling, so some distortion of the cavity mode occurred. There is also significant distortion from the finite number of holes. This distortion extends into the beam region, and there is concern that this could result in uneven beam bunching. The obvious solution is a continuous slot; however, unlike the short slots, this does not form a cutoff waveguide. It was found that controlling the coupling was very difficult. An additional difficulty is that the output waveguide itself is overmoded. A taper would be required to transition to WR-90 guide. If any high order modes were excited from either forward or backward scattering, they would be trapped in the taper. This could produce anomalies in the gain curve and (if used as an output coupler) loss in efficiency and/or breakdown.

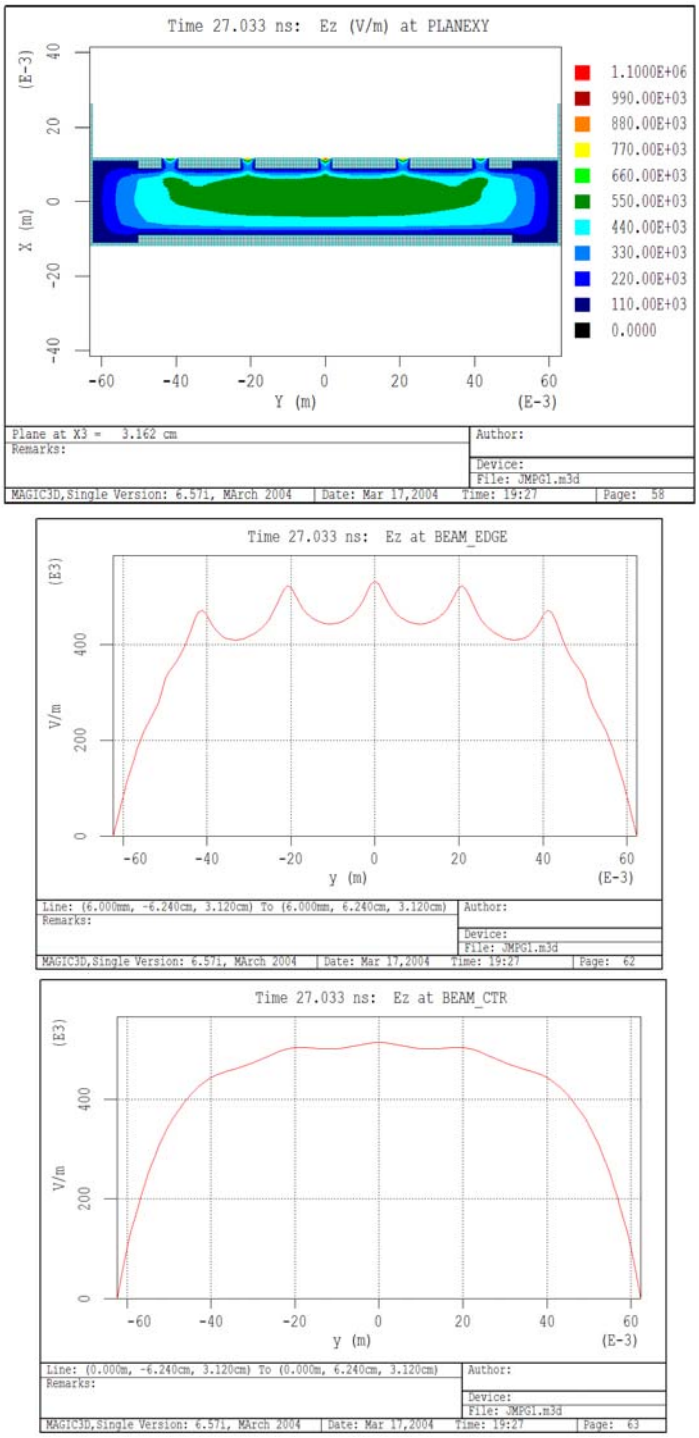

Figure 38. Simulations with a five-slot coupler. Top: Geometry and mode pattern in the XY plane of the center cell of a three-cell cavity. The waveguide extends from the top of the cavity. Middle: Ez along Y at the edge of the drift guide. Bottom: Ez along Y at the center of the beam.

This problem can be avoided by using coupling to the sidewall of a fundamental waveguide as shown in Figure 39b. Unfortunately this approach limits the number of slots that can be used as they must be spaced by the guide wavelength in the fundamental mode output waveguide. For the output cavity width, this limits the maximum coupling slots to three. To get sufficient coupling into the cavity the slots must be made larger, resulting in more field distortion. Beam simulations can determine the loss in efficiency resulting from this beam distortion.

Coupling from the end walls (re-entrant sections of cavity) will provide the minimum distortion to the cavity field. This approach has a couple of difficulties also. Only two coupling slots are possible when coupling to the center cavity, and it is also required that the power be recombined into one waveguide. This configuration may result in excessive electric fields in the output coupler. The number of coupling slots can be increased to four if coupling to the outer cavity sections, but this requires recombing the four output ports into one.

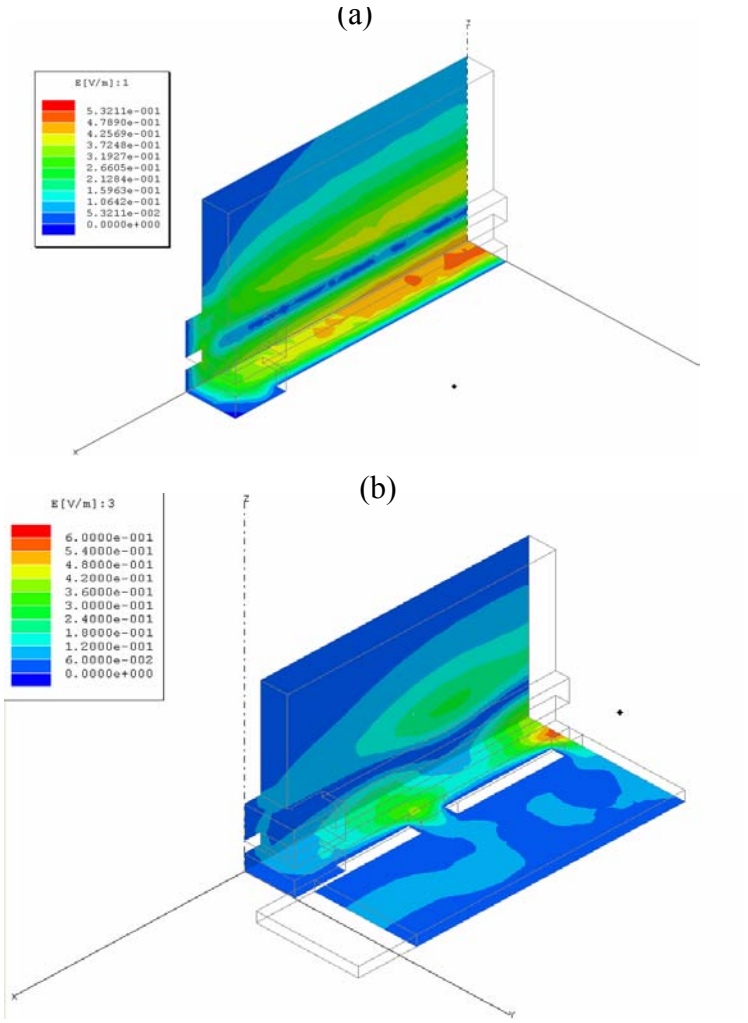

Figure 39. Field intensity for output cavity circuit modeled with 1/8 of total cavity volume. (a) Unperturbed cavity. (b) Cavity with coupling to sidewall of fundamental mode waveguide. The resonant frequency and Q were 11.488 GHz and 512, respectively.

Initial calculations were performed for both the side and end wall configurations. The calculation for the sidewall coupler is shown in Figure 39b along with the unperturbed cavity for comparison. These calculations used Ansoft's High Frequency Structure Simulator (HFSS) program. It can be seen that the coupling slots between the cavity and the waveguide distort the fields in the cavity. It is likely these distortions would degrade the interaction efficiency.

A calculation for the output cavity with an end wall coupler is shown in Figure 40. There is significantly less distortion of the field profile in the cavity. The field uniformity can be further improved by fine tuning the cavity dimensions; however, there is an enhancement of the field along the sharp corners at and near the output iris. The field levels are 10-15 MV/meter for a 50 MW output. This field level is acceptable for the short pulse operation and can be reduced further by smoothing the sharp corners.

The end wall coupler appears to be the better approach for extracting the RF from the output waveguide. The enhancement of the field near the iris can be reduced to an acceptable level. Good field uniformity across the beam is achievable, and the field profile can be tailored by adjustment of the cavity and re-entrant section parameters. The endwall coupler requires a power combiner, but this is routinely implemented for two waveguides. Consequently, the Phase II cavity design will implement the end wall approach.

A final calculation for the input cavity is shown in Figure 41. Very little distortion of the field occurs, since the design Q is much higher than for the output cavities. The enhancement of the field near the iris will not be an issue since the input power is very low.

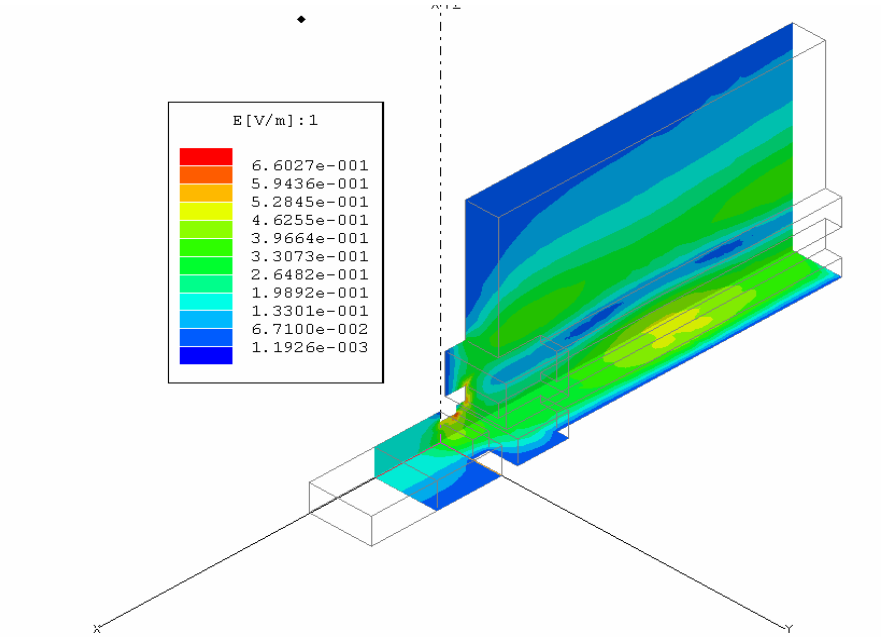

Figure 40. Field intensity for output cavity circuit with end wall coupling. The resonant frequency and Q for this case were 11.450 GHz and 310 respectively.

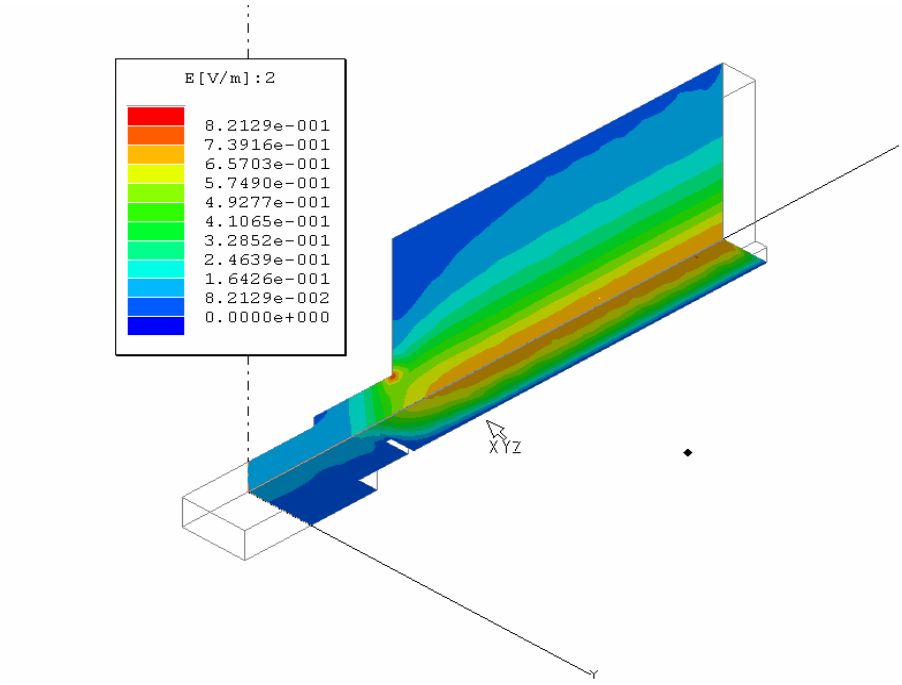

Figure 41. Field intensity for input cavity circuit with end wall coupling. The resonant frequency and Q for this case were 11.40 GHz and 1040 respectively

Collector

The low beam current density makes the collector straightfoward. A preliminary design is shown in Figure 42.

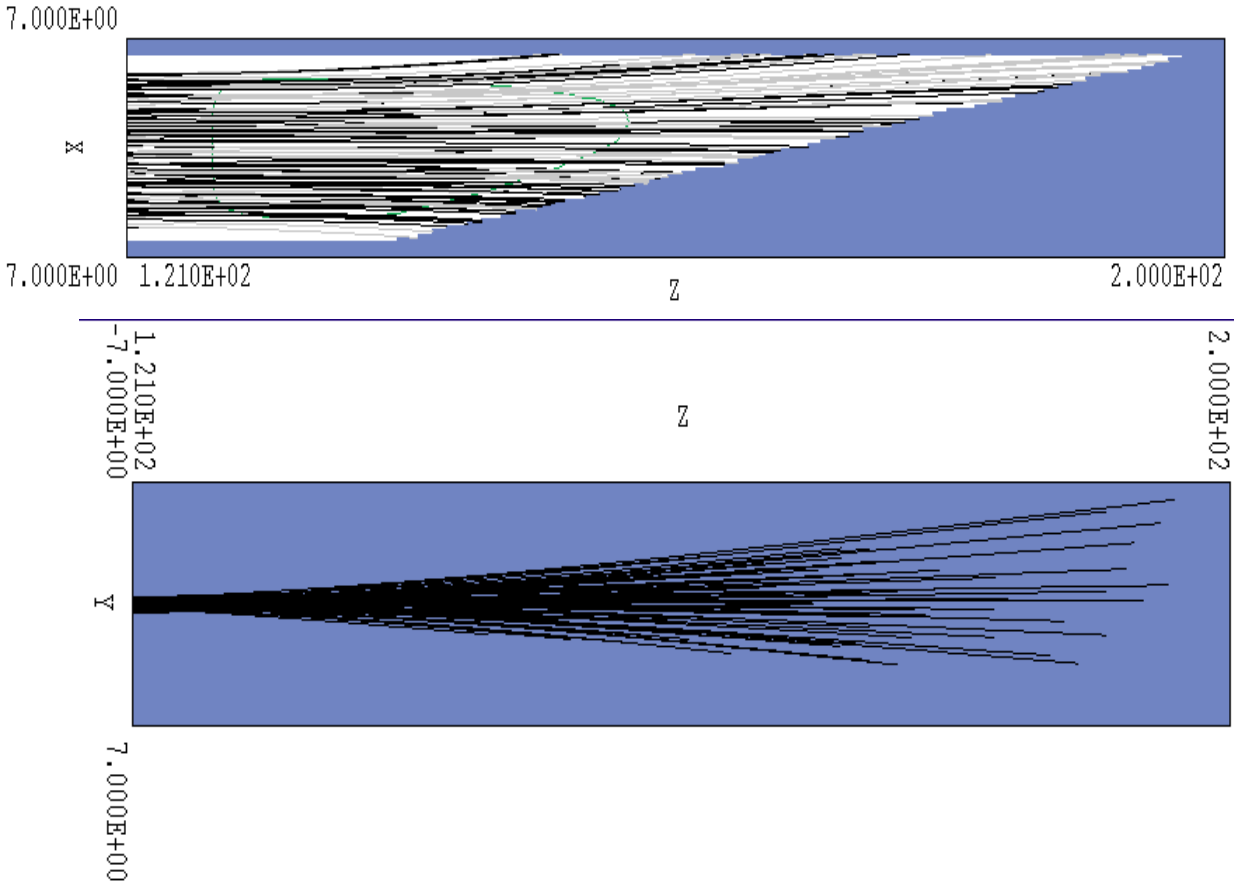

Figure 42. Cross sections of the collector. Top: XZ. Bottom: YZ.

The distribution of particles (each with a current of 0.5A) is shown in Figure 43. The current distribution projected onto the YZ plane is shown in Figure 44. For a duty factor of 3.8 10^{-4}, corresponding to 3.2 μs pulses at 120 Hz, the average power density is 350 W/cm^2. This is well within acceptable values. The maximum peak power is 920 kW/cm^2, which should be acceptable for sub-microsecond pulses. Pulse widths up to the maximum required 3.2 μs can be achieved by additional shaping near the end of the collector. This will be straightforward.

.,

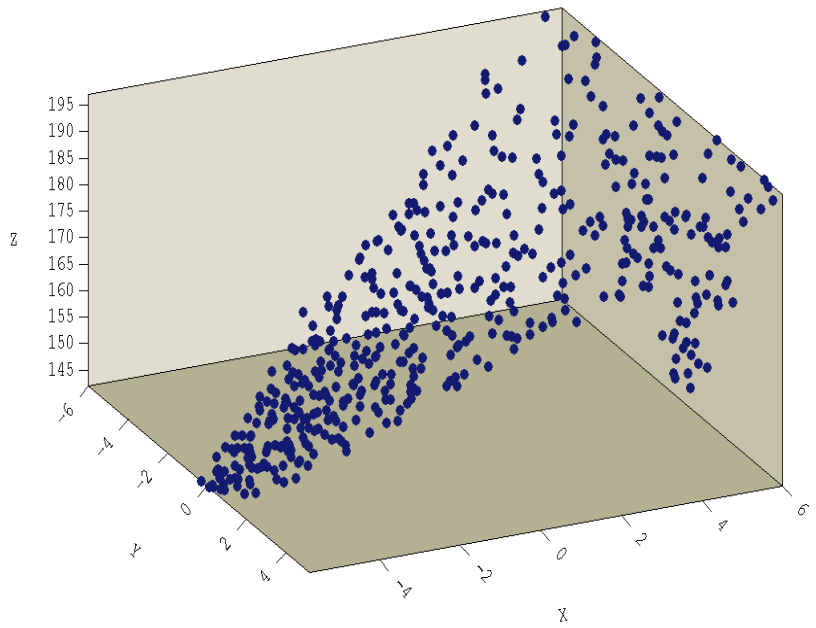

Figure 43. Scatter plot of the termination positions of the trajectories. Each point represents 0.5 A or 207 kW peak power and 80 W average power.

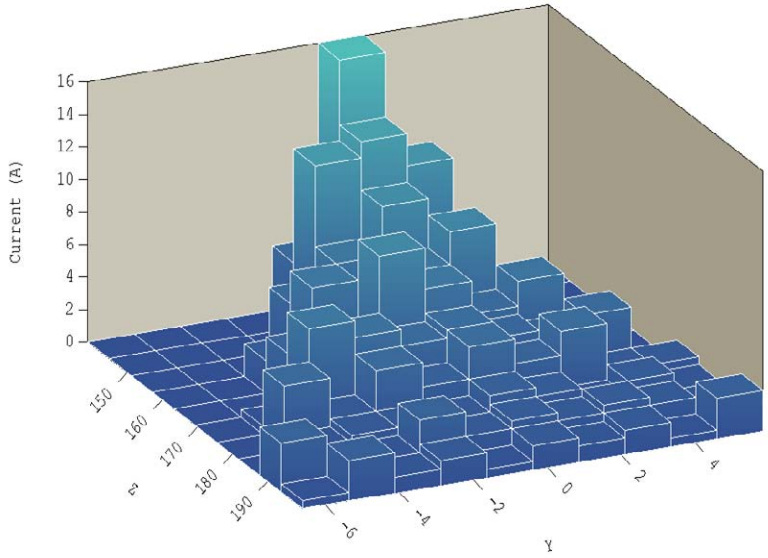

Figure 44. Current distribution projected onto the YZ plane. Each bin has an area of 7.2 cm^2, and thus the peak current density is 2.2 A/cm^2, or 920 kW/cm^2. The maximum average power is 350 W/cm^2.

3. Conclusions and Recommendations

The Phase I results clearly demonstrated feasibility of the sheet beam klystron. The two issues of most concern were mode competition and PPM transport of the electron beam through the circuit. Theoretical calculations and computer simulations indicate that no competing modes will inter-

fere with klystron operation. Simulations of the PPM focusing structure indicate that excellent beam propagation can be achieved, provided a good quality electron beam is provided by the gun. The Phase I program was particularly useful in generating additional specifications for the electron gun to ensure proper operation for PPM transport. This information can be used to optimize the design of the electron gun.

While good performance of the klystron is demonstrated, it is anticipated that improved performance can be achieved with further optimization.

4. References

[1] A. Staprans, "Electron Gun Breakdown," High Voltage Workshop, Monterey, 1985.

[2] K.S. Fant, G. Caryotakis, R.F. Koontz and A.E. Vlieks, "High Gradient Electron Guns," SLAC-PUB-5325 (1990).

[3] J. H. Booske, M. A. Basten, A. H. Kumbasar, T. M. Antonsen, Jr., S. W. Bidwell, Y. Carmel, W. W. Destler, V. L. Granatstein, and D. J. Radaqk, "Periodic magnetic focusing of sheet electron beams," Phys. Plasmas 1 (5), pp. 1714-1720 (1994).

[4] J.H. Booske, B.D. McVey and T.A. Antonsen, "Stability and Confinement of Nonrelativistic Sheet Electron Beams with Periodic Cusped Magnetic Focusing," J. App. Phys. 73(9), pp. 4140-4155 (1993).

[5] M.A. Basten and J.H. Booske, "Two-Plane Focusing of High Space Charge Electron Beams Using Periodically Cusped Magnetic Fields," J. App. Phys. 85(9), pp. 6313-6322 (1999).

[6] R. True, "A Theory for Coupling Gridded Gun Design with PPM Focusing," IEEE Trans. Elect. Dev., ED-31(3), pp. 353-362 (1984).

[7] J.R. Pierce Theory and Design of Electron Beams," D. Van Nostrand Co., Inc. (1954).

[8] G. Caryotakis, personal communication (2003).

[9] G. Caryotakis, D. Sprehn, E. Jongewaard, M. Neubauer, D. Martin, G. Scheitrum, "SLAC Sheet Beam Klystron Design Issues," Multi-disciplinary University Research Initiative Teleconference, November 7, 2001. Research supported by AFOSR MURI contract 99A0734-04, AFRL MIPR NAFRL006202117, and by Department of Energy contract DE-AC03-76SF00515.

[10] B.E. Carlston, S.J. Russel, L.M. Earley, J.M. Potter, P. Ferguson, and S. Humphries, Jr., "MM-Wave Source Development at Los Alamos," Proc. High Energy Density and High Power RF: 6th Workshop, ed. S.H. Gold and G.S. Nusinovich, pp. 349-357 (2003).

[11] G.S. Nusinovich, M.E. Read, L. Song and R.L. Ives, "Self-Excitation Conditions in Overmoded Klystrons," to be presented at IVEC 2004, Monterey, CA.(2004).